3D porous catalysts for plasma-catalytic dry reforming of methane : how does the pore size affect the plasma-catalytic performance?

3D Porous Catalysts for Plasma-Catalytic Dry Reforming of Methane: How Does the Pore Size Affect the Plasma-Catalytic Performance?

Jinxin Wang[a,b], Kaimin Zhang[b], Annemie Bogaerts[a]* and Vera Meynen[b,c]*

[a]Plasma Lab for Applications in Sustainability and Medicine - ANTwerp, Department of Chemistry, University of Antwerp, Universiteitsplein 1, 2610 Wilrijk, Antwerp, Belgium
[b]Laboratory of Adsorption and Catalysis, Department of Chemistry, University of Antwerp, Universiteitsplein 1, 2610 Wilrijk, Antwerp, Belgium
[c]Flemish Institute for technological research, VITO NV, Boeretang 200, 2400 Mol, Belgium

*Email: annemie.bogaerts@uantwerpen.be; vera.meynen@uantwerpen.be

Abstract

The effect of pore size on plasma catalysis is crucial but still unclear. Studies have shown plasma cannot enter micropores and mesopores, so catalysts for traditional thermocatalysis may not fit plasma catalysis. Here, 3D porous Cu and CuO with different pore sizes were prepared using uniform silica particles (10–2000 nm) as templates, and compared in plasma-catalytic dry reforming. In most cases, the smaller the pore size, the higher the conversion of CH_4 and CO_2. Large pores reachable by more electrons did not improve the reaction efficiency. We attribute this to the small surface area and large crystallite size, as indicated by N_2-sorption, mercury intrusion and XRD. While the smaller pores might not be reachable by electrons, due to the sheath formed in front of them, as predicted by modeling, they can still be reached by radicals formed in the plasma, and ions can even be attracted into these pores. An exception are the samples synthesized from 1 μm silica, which show better performance. We believe this is due to the electric field enhancement for pore sizes close to the Debye length. The performances of CuO and Cu with different pore sizes can provide references for future research on oxide supports and metal components of plasma catalysts.

Keywords: Plasma catalysis; Dry reforming; 3D porous catalysts; Effect of pore size; Dielectric barrier discharge reactor

1. Introduction

Plasma catalysis is considered a promising alternative to various traditional chemical processes, such as the decomposition of gaseous pollutants and the synthesis of organic chemicals [1-3]. CO_2 reforming of methane (dry reforming) is one of the attractive processes among them since it simultaneously utilizes two greenhouse gases (CH_4 and CO_2), which can come from sustainable resources such as biogas, to produce fuels and chemical products [4-9]. Due to the low chemical reactivity of CH_4 and CO_2, the classical thermocatalytic reaction requires a high temperature (at least 800 °C) to provide sufficient energy to activate them, which leads to problems like energy loss and deactivation of the catalysts [10-15]. These problems can be overcome by non-equilibrium plasma, since it allows the reaction to proceed at relatively low temperatures (lower than 250 °C) [16-18]. The high-energy electrons produced by plasma can break the stable chemical bonds of CH_4 and CO_2, while the gas molecules themselves can remain close to room temperature, hence the term "non-equilibrium plasma" [19-21]. A popular type of

42 non-equilibrium plasma reactor is the dielectric barrier discharge (DBD) reactor, which is
43 straightforward to be combined with a catalyst. Moreover, it is easily to be applied in the
44 chemical industry because it can be operated at ambient temperature and atmospheric pressure
45 [22-26].

46 A DBD reactor operating in CO_2/CH_4 mixtures is typically in filamentary discharge mode,
47 composed of a large number of independent micro-discharge filaments, which is greatly affected
48 by the size and geometry of the reactor, as well as by the packing materials and catalysts filled in
49 the reactor [27-30]. Therefore, the interaction between the plasma and the catalyst must be taken
50 into account to study the plasma-catalytic dry reforming, not only the reaction process of feed gas
51 molecules and the catalyst. Moreover, the reactant gas in the plasma state may exhibit quite
52 different properties than in thermal reactions. Hence, the role played by the catalysts is more
53 complicated than in thermal catalysis and is still not entirely clear.

54 The catalysts used in the existing studies are often the same as or slightly modified from the
55 catalysts for traditional thermocatalytic dry reforming. Some studies reported that the catalyst had
56 a synergistic effect with the plasma to promote the conversion of CH_4 and CO_2. For example,
57 Vakili et al. [31] deposited Pt nanoparticles on the metal-organic framework material UiO-67
58 MOF as a catalyst, which enhanced the conversion of CH_4 and CO_2 in the diluted feed gases
59 (5000 ppm). Zeng et al. [32] studied γ-Al_2O_3 supported transition metals (Ni, Mn, Co, Cu), and
60 found that compared with only plasma in an empty reactor, filling pure γ-Al_2O_3 or γ-Al_2O_3
61 supported transition metal catalysts in the reactor yielded an improvement in the conversion of
62 CH_4 (maximum increase was from ~14% to ~20%), although the conversion of CO_2 slightly
63 decreased (from ~10% to ~9%). However, more studies showed inverse effects of the catalysts on
64 plasma dry reforming, especially for those experiments using undiluted feed gases [33,34]. Wang
65 et al. [18] also used a γ-Al_2O_3 support loaded with the same transition metal Cu as Zeng et al..
66 Moreover, also noble metals (Au, Pt), which are generally considered to be more active for dry
67 reforming, were used as active ingredients [18,35]. However, due to the inhibition of the
68 discharge by the catalysts, both the γ-Al_2O_3 with and without supporting metals reduced the
69 conversion of CH_4 and CO_2 compared to the plasma reaction in an empty reactor, although the
70 selectivity of some products was improved. Michielsen et al. [36] and Andersen et al. [37]
71 reported that if keeping the same space time as the empty DBD reactor, packing materials and
72 catalysts do have positive effects on the dry reforming (DRM) reaction. However, the (catalytic)
73 packing material decreased the discharge volume in the reactor, leading to a shorter space time in
74 the plasma. For some materials, the promotion of the DRM reaction due to the catalytic activity
75 or electric field enhancement of the packing could not compensate for the decreased conversion
76 caused by the loss in volume. In short, since there are so many factors affecting the interaction
77 between catalyst and plasma, a wide variety of very different research results on plasma-catalytic
78 dry reforming have been published in literature, even for similar packing materials. However, a
79 general observation is that the majority of porous catalysts did not show an improvement in
80 plasma catalysis [38].

81 In order to study how porous materials affect the plasma in a DBD reactor, some researchers
82 have simulated the behavior of plasma streamers in catalyst pores. Zhang et al. [39-42] studied by
83 modeling whether plasma can enter catalyst pores. Their simulations showed that plasma could
84 only be generated or penetrate into pores that are larger than the so-called Debye length, which is
85 hundreds of nanometers at typical plasma-catalytic conditions. However, the porous materials
86 applied as catalyst supports in the existing plasma-catalytic dry reforming studies were usually
87 only with micropores or mesopores smaller than 10 nm. Hence, these are much smaller than the
88 pore size in which plasma can be formed. Although microporous or mesoporous materials show
89 good performance in traditional thermocatalytic dry reforming, because of their large specific

90 surface area, the surface area resulting from the small pores might be ineffective for plasma
91 reactions according to the simulation of Zhang et al. However, if the micropores and mesopores
92 were ineffective for plasma reactions, the question arises what then caused the improved
93 conversion in plasma-catalytic dry reforming, reported in those papers applying microporous or
94 mesoporous catalysts?

95   In many papers, only part of the DBD reactor space was packed with a little catalyst, to
96 promote conversion of dry reforming by catalysts, although they might not mention or study this
97 [32,43,44]. Tu et al. reported that instead of packing the catalyst particles into the entire discharge
98 gap, packing a small amount of catalyst into a part of the gap improved the conversion of dry
99 reforming [38]. Ray et al. studied the performance of Ni-Mn/γ-Al$_2$O$_3$ bimetallic catalyst for dry
100 reforming, and found that the reactant conversion of full catalyst packing and 50% catalyst
101 packing in a DBD reactor were similar to or even worse than that without catalyst, while 25%
102 catalyst packing showed the best performance among all conditions [45]. They suggested that the
103 reduction of discharge in DBD reactors, resulting from catalyst particle packing, is the reason that
104 a partially packed or empty reactor has better performance than a full catalyst packed one.
105 Furthermore, the conclusion of Zhang et al. [39-42] that the plasma cannot enter or be formed in
106 the pores of microporous or mesoporous materials (e.g. γ-Al$_2$O$_3$) is another reason that a catalyst
107 packing greatly reduces the plasma volume. It is reasonable that the more catalyst filling, the
108 greater the negative effect on the plasma reaction. However, the dry reforming performance of
109 some partially packed reactor (e.g. 25% Ni-Mn/γ-Al$_2$O$_3$ packing) is better than that of an empty
110 reactor, which implies that the catalyst also has a positive effect on the plasma dry reforming in
111 some way, even if the pores are unreachable to plasma. There is a balance between this positive
112 effect and the negative effect of catalyst packing, which is the reason for the better conversion in
113 partially packed reactors. However, this partial packing method is a compromise between catalyst
114 and plasma. It reduces the negative effect of catalyst on the plasma, but also means that neither
115 the plasma nor the catalyst can be fully utilized. Since one of the negative effects of catalysts on
116 plasma is caused by the small pore size, a potential way is to apply catalysts with larger pores into
117 which the plasma can enter, to see if it can maintain the positive effects of the catalysts while
118 decreasing the negative effects of catalyst particles on plasma discharge. In addition, although the
119 micropores and mesopores are ineffective for plasma discharge, their comprehensive effects on
120 the plasma dry reforming processes are unknown. In order to truly combine the advantages of the
121 catalyst and plasma reaction, and to know the right future research direction of the catalyst for
122 plasma reactions, it is crucial to study the role of catalyst pores and the effect of pore size in
123 plasma-catalytic dry reforming.

124   Some studies compared different catalyst supports that may possess different pore sizes, but
125 they were limited to materials with pores of a few nanometers, while the larger plasma-reachable
126 pores have rarely been studied [46-48]. Moreover, since the difference in materials, structures and
127 properties of different supports resulted in too many interference factors, it is impossible to
128 conclude the effect of the pore size on plasma dry reforming from these studies.

129 In the present paper, we thus synthesized catalysts of the same material with different pore sizes
130 in the range of a few nanometers to micrometers and studied their performance for dry reforming
131 in a DBD plasma reactor. Since the common porous supports or porous structure preparation
132 process cannot adjust the pore sizes in such a large span, silica spheres with different diameters
133 were prepared first as templates and then removed by etching to get 3D porous catalysts with
134 different and controlled intraparticle pore sizes, as shown in Figure 1. The size of interparticle
135 voids resulting from particle packing is not the focus of this work and did not vary significantly
136 between samples. In existing studies, various metals, such as Pt, Au, Rh, Ru, Cu, Ni, etc., are
137 typical active components of plasma dry reforming catalysis [18,37,45,49]. Noble metals usually

138 have higher catalytic activity, but considering the cost of these catalysts and their presence on the
139 critical raw material list, more abundant metals such as Cu and Ni are more promising research
140 targets. In this work, copper was applied as the metal active ingredient, and unreduced copper
141 oxide was also investigated as an example of a material with a certain dielectric constant. The
142 porous structured samples consisted of pure copper or copper oxide without any support, so the
143 influences of the supports (e.g. metal-support effects, alkalinity of the supports) do not have to be
144 considered in this study, in contrast to literature studies using porous supported catalysts.

145
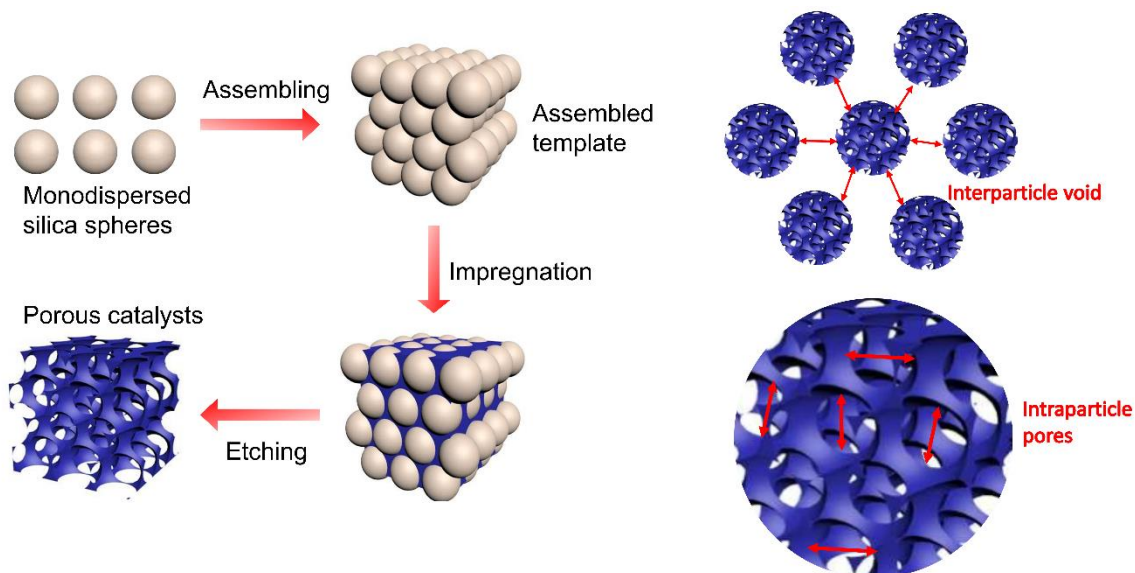
146

147 Figure 1. The process for the 3D porous catalysts synthesis (left), and explanation of the interparticle voids and
148 intraparticle pores (right).

149 2. Experimental

150 2.1. Preparation of the 3D porous catalysts

151   Ammonia solution (wt % = 25 %), tetraethyl orthosilicate (TEOS) and ethanol were purchased
152 from Sigma-Aldrich. Copper nitrate trihydrate was purchased from Acros.

153 2.1.1. Preparation of SiO_2 spheres template

154   The silica spheres were synthesized by a modified Stöber method from our previous study
155 [50]. A certain amount of ammonia solution was dissolved in deionized water. The solution was
156 agitated gently at 20 °C and 200 mL tetraethyl orthosilicate was added into it. Then, we kept
157 stirring the mixture at the same temperature for 24 h. The silica spheres were obtained after
158 centrifugation and drying at 80 °C for 24 h. The different ratios of ammonia to water were used to
159 adjust the diameter of the silica spheres. Silica particles with diameters of about 10 nm, 50 nm,
160 100 nm, 600 nm, 1 and 2 μm were synthesized as templates for the next step of impregnation.

161 2.1.2. Impregnation and etching of metal ingredients

162   The silica samples were calcined at 800 °C for 12 h to interconnect the spheres. Excess copper
163 nitrate (twice the mass of silica) was dissolved in ethanol and subsequently the silica was added.
164 The mixture was left without agitation for 48 hours to complete the impregnation. Then, the solid

165 product was dried in an oven at 80 °C for 24 h. The resulting sample was calcined in a crucible at
166 650 °C to decompose the nitrate species. Finally, the silica template was removed by etching with
167 2 M NaOH aqueous solution at 80 °C for 5 h. After washing to neutral and drying at 80 °C, the
168 3D porous metal oxide was obtained.

169 The samples were denoted by the diameter of the silica particles used in the impregnation. For
170 example, copper oxide synthesized using 10 nm and 2.5 µm silica particles as templates were
171 denoted as CuO-10 and CuO-2500, respectively, and if reduced with H_2 before plasma testing,
172 the catalysts are denoted as Cu-10 and Cu-2500, respectively.

2.2. Characterization of the catalysts

174 X-ray powder diffraction (XRD) was applied to characterize the crystal phases of all the CuO
175 samples. The measurements were performed by a D8 advance Eco diffractometer with Cu-Kα
176 radiation (λ= 1.5406 Å) at a scanning range of 10–80° 2θ and a scanning rate of 0.04°/4 s. The
177 XRD patterns of all the samples were normalized by dividing every peak by the most intense
178 peak to get relative intensities.

179 The scanning electron microscopy (SEM) and energy dispersive X-ray spectroscopy (EDX)
180 were used to investigate the topography and surface composition of the samples. They were
181 carried out by the FEI Quanta ESEM FEG 250 field emission microscope with an EDX detector
182 operating at 20 kV.

183 Nitrogen sorption was used to study the pore size (< 50 nm) and specific surface area of the
184 samples. The measurements were carried out on a Quantachrome Quadrasorb SI automated gas
185 sorption system. The samples were degassed for 16 h under high vacuum at 200 °C before the N_2-
186 sorption measurements. The temperature was kept at -196 °C by liquid nitrogen during the N_2-
187 sorption. The surface area was determined by the multi-point Brunauer–Emmett–Teller (BET)
188 method and the pore size distribution was determined by non-local density functional theory
189 (NLDFT) on the adsorption branch.

190 Mercury porosimetry was applied to study the macropores (> 50 nm). The mercury
191 porosimetry was executed on a Themo Electron Corporation Pascal 140 + 240 series, operating in
192 2 different pressure regimes. Prior to mercury intrusion the samples were vacuum dried for 10
193 minutes.

194 Diffuse reflectance infrared Fourier transform (DRIFT) spectrometry was performed with a
195 resolution of 4 cm^{-1} and the accumulation of 100 scans, on a Nicolet 6700 Fourier Transform IR
196 spectrometer, to study the surface groups of the CuO samples. The samples for the measurements
197 were diluted by KBr to 0.5 wt%, and pure KBr was used as a background. The spectra were
198 obtained after stabilizing for 30 min with 80 mL/min of Ar flushing at room temperature.

199 Hydrogen-temperature programmed reduction (H_2-TPR) and oxygen-temperature programmed
200 oxidation (O_2-TPO) were combined to check if the CuO samples were reduced completely in the
201 tube furnace when Cu was needed for the dry reforming test. The measurements were carried out
202 on the ChemStar TPX Chemisorption Analyzer. First, the samples were degassed at 350 °C for 2
203 h with 50 mL/min pure He flushing. After cooling down to 50 °C, the first O_2-TPO was carried
204 out from 50 °C to 800 °C with 10 °C/min ramping rate, under 5% O_2/He at a flow rate of 50
205 mL/min. After cooling down to 50 °C again, the H_2-TPR was performed to 800 °C with
206 10 °C/min ramping rate, under 50 mL/min of 5% H_2/Ar. The second O_2-TPO was done with the
207 same procedure as the first one after cooling down.

208   Thermogravimetric analyses (TGA) were performed on a Mettler Toledo TGA-DSC 3+ in a
209 continuous 80 mL/min flow of O_2. A heating rate of 10 °C/min from 30 °C to 800 °C was applied.

2.3. Plasma-catalytic performance test of the catalysts

211 2.3.1. Set-up of the DBD reactor

212   A fixed bed DBD reactor as illustrated in Figure 2 was applied to study the plasma-catalytic
213 performance for dry reforming of the catalysts with different pore sizes. The inner electrode was a
214 stainless steel rod with outer diameter of 13 mm. An alumina dielectric tube with 21.8 mm outer
215 diameter and 17.41 mm inner diameter was coaxially placed over the stainless steel rod as a
216 dielectric barrier, so the discharge gap between the inner electrode and dielectric barrier was
217 about 2.2 mm. A stainless steel mesh was used as outer electrode by tightly winding it on the
218 outside of the alumina tube. The length of the outer electrode, which determines the length of the
219 discharge zone, was 10 mm. 4 g of catalyst powder was filled in the whole plasma zone with 2 g
220 glass wool at both sides to fix the powder. The tapped volume of 4 g of samples was larger than
221 the volume of the discharge space (1.05 mL), to avoid the possible effect of glass wool on both
222 sides on the discharge. Moreover, in order to measure the weight filled in the discharge space to
223 calculate the packing density, the particles were repacked in an amount that just fills the discharge
224 space of the reactor.

225   The inner electrode was grounded, and the outer electrode was connected to a high voltage
226 supplied by a function generator (Tektronix, AFG 2021) and a high voltage amplifier (TREK,
227 Model 20/20C-HS). The generator provided a signal with a frequency of 3000 Hz, and the
228 amplifier amplified the input signal by 2000. A high-voltage probe (Tektronix, P6015A) was used
229 to measure the voltage, and a Rogowski coil (Pearson 4100) was used to monitor the current. The
230 current profile was filtered by applying a Savitzky-Golay filter of polynomial order 3 to exclude
231 the signal noise [28]. The number of peaks per period in the current profile, after excluding signal
232 noise, was used to study the number of micro-discharges in this study. It should be noted that this
233 is not the exact number of discharges that occurred in the reactor, since the discharges might have
234 occurred simultaneously, while only one peak of current was shown in the current profiles. In
235 addition, some small discharges might be excluded as signal noise. However, multiple collections
236 of current data and an average value of the number of current peaks can be used to compare and
237 study the effects of different samples on the discharge even though the obtained numbers should
238 not be interpreted as absolute but as apparent values. The charge in the plasma was monitored by
239 a capacitor (10 nF) connected in series and a low-voltage probe (Picotech, TA150) connected in
240 parallel with it. The displaced charge was obtained from it by taking the detected charge
241 difference before and after discharge. All the signals were collected by an oscilloscope (Picotech,
242 Picoscope 6402D) and shown on a PC. The data was calculated in real time to adjust the
243 amplitude of the input signal from the amplifier, in order to keep the power of the power supply
244 constant at 50 W. The calculation and counting of electrical parameters are done automatically by
245 a MATLAB script.

246 2.3.2. Catalyst performance evaluation

247   The copper oxide was filled and tested directly in the reactor. However, to evaluate the copper
248 samples, the copper oxide powder was reduced in a tube furnace (Carbolite Gero TF1 12/60/300)
249 with 250 mL/min of 2% H_2/Ar gas flow at 450 °C for 8 h before being packed into the reactor.
250 The reduction temperature of CuO was 450 °C which is determined by H_2-TPR.

For the plasma-catalytic dry reforming test, the feed gas consisted of 5 mL/min of CH_4 and 5 mL/min of CO_2, and the flow rate was controlled by mass flow controllers (Bronkhorst EL-FLOW Select). 10 mL/min of N_2 was added in the outlet gas as internal standard to exclude the impact of the gas expansion. The product gases from the reactor outlet were analyzed by an online gas chromatograph (Trace GC 1310, Interscience) equipped with a thermal conductivity detector (TCD) and a flame ionization detector (FID). Thermocouples were used to measure the temperature of the external electrodes and the gas at the outlet (about 10 cm from the discharge space) of the reactor. In all our experiments, the gas temperature at the outlet of the reactor was about 20–25 °C, and the temperature of the external electrode was about 50 °C. Also, Van Turnhout et al. recently presented a novel method to determine the temperature of the catalyst surface, and revealed that the plasma-induced temperature rise in a DBD reactor is limited ($\leq$ 150 °C) [51]. It might always be possible that the temperature in the reactor is higher at some places (local hot spots) and dependent on the type of packing material and operating conditions; however, since thermal dry reforming hardly takes place below 300 °C [38], we can consider that the conversion of CH_4 and CO_2 in our reactor is mainly due to the plasma reaction. After flushing the filled reactor with the feed gas for 30 minutes without plasma, the composition of the outlet gas was analyzed and recorded as blank measurements, and the amount of CO_2 and CH_4 were denoted as $CO_{2,in}$ and $CH_{4,in}$ respectively. Then, the power was applied to generate plasma, and kept at 50 W for 30 minutes. The gases generated and unconverted feed gas after 30 min were analyzed and their amounts were marked with "out", i.e., $CO_{2,out}$, $CH_{4,out}$, $H_{2,out}$, CO_{out} and $C_xH_yO_{z,out}$. The conversion of CO_2 and CH_4 are calculated by Eq. (1) and Eq. (2)

$$X_{CO_2} = \frac{CO_{2,in} - CO_{2,out}}{CO_{2,in}} \cdot 100\% \tag{1}$$

$$X_{CH_4} = \frac{CH_{4,in} - CH_{4,out}}{CH_{4,in}} \cdot 100\% \tag{2}$$

The selectivity (S) of the products are defined by Eq. (3) to Eq. (5)

$$S_{H_2} = \frac{H_{2,out}}{2 \times (CH_{4,in} - CH_{4,out})} \cdot 100\% \tag{3}$$

$$S_{CO} = \frac{CO_{out}}{(CH_{4,in} - CH_{4,out}) + (CO_{2,in} - CO_{2,out})} \cdot 100\% \tag{4}$$

$$S_{C_xH_yO_z} = \frac{x \times C_xH_yO_{z,out}}{(CH_{4,in} - CH_{4,out}) + (CO_{2,in} - CO_{2,out})} \cdot 100\% \tag{5}$$

The energy yield (EY) of the reaction was defined as the amount of CO_2 and CH_4 that can be converted per kJ of input energy, as shown in Eq. (6)

$$EY \text{ (mmol/kJ)} = \frac{(V_{CO_2}X_{CO_2} + V_{CH_4}X_{CO_4})}{PV_m} \cdot \frac{1000}{60} \left(\frac{Wmin}{kJ}\right) \tag{6}$$

Where V_{CO2} and V_{CH4} are the volumetric flow rate (in mL/min) of CO_2 and CH_4 in the feed gas. V_m is the molar gas volume (24.4 mL/mmol) and P is the plasma power (in W). The factor 1000/60 (Wmin/kJ) is to convert the unit from Wmin to kJ.

The DRM reaction produces CO, H_2 and various hydrocarbon products, resulting in the expansion with an unknown coefficient and pressure rise of the outlet gases. The GC always depressurizes the gases to ambient pressure during sampling, so the direct calculation of

287   conversion and selectivity from gas_{out} and gas_{in} obtained by the GC will have systematic errors.

288   Therefore, 10 mL/min N_2 flow was applied as the internal standard to reduce the errors [52].
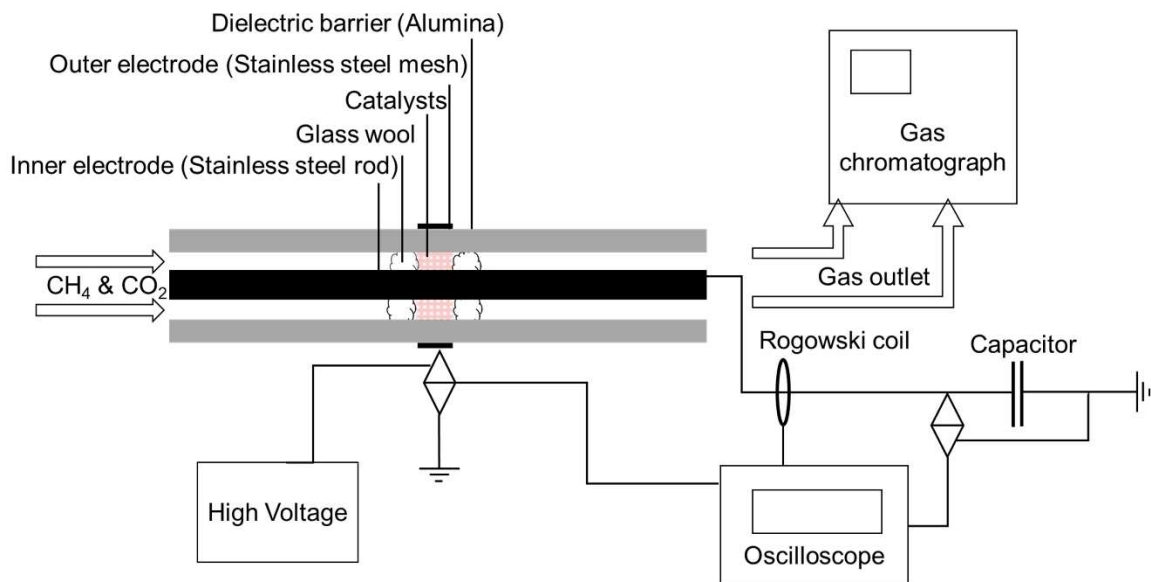
289

290   Figure 2. DBD reactor setup for the dry reforming of methane.

291   **3. Results and discussion**

292   **3.1. Structure and properties of the catalysts**

293   The normalized XRD patterns of the 3D porous CuO samples, synthesized from silica

294   particles of different sizes, are shown in Figure 3, and the original XRD patterns are shown in

295   Figure S1 in Supplementary Material. A sample with copper oxide loading but without etching

296   away the SiO_2 is also characterized by XRD for comparison. It is obvious that a broad peak

297   attributed to (111) reflection of SiO_2 is detected at $2\theta = 21.60°$ in the sample without etching,

298   while it is no longer present in all etched porous copper oxide samples. The diffraction peaks at

299   other angles, such as the peaks at $2\theta = 32.51°, 35.42°, 38.71°, 48.72°, 53.49°, 61.52°, 66.22°,$

300    $68.12°, 72.37°,$ and $74.98°$ are indexed to the (1 1 0), (0 0 2), (1 1 1), (2 0 -2), (0 2 0), (1 1 -3), (3

301   1 -1), (2 2 0), (3 1 1), and (0 0 4) crystal planes of Tenorite CuO (JCPDS 48-1548). These peaks

302   get sharper with the increase of particle size of the applied SiO_2 template during the syntheses

303   (from CuO-10 to CuO-600), suggesting that the crystallinity and crystallite size of CuO is getting

304   higher owing to the CuO sintering by calcination at 650 °C. When smaller silica particles are used

305   as templates, the gaps between the particles are smaller, which restricts the growth of crystallites,

306   resulting in smaller grains of copper oxide and thinner pore walls. On the contrary, thicker pore

307   walls and larger copper oxide crystallites are obtained when larger silica particles are used as

308   templates. The crystallinity and crystallite size of the CuO-600, CuO-1000 and CuO-2000 is

309   similar, and no longer increase significantly with increasing particle size of the SiO_2 template.

310
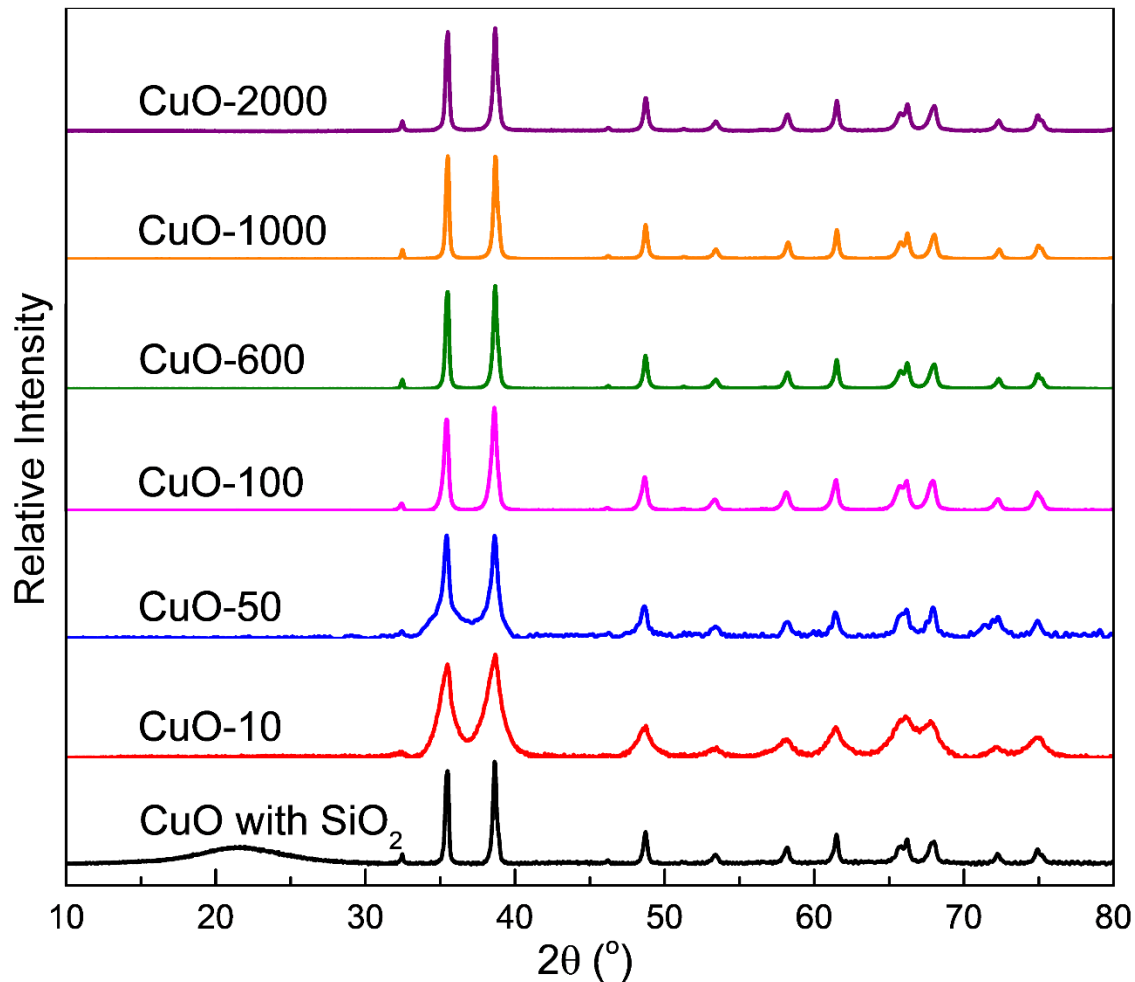
Figure 3. The normalized XRD patterns of the 3D porous CuO samples.

SEM measurements were carried out to observe the morphology and pore sizes of the 3D porous CuO samples, and the images are shown in Figure 4. All the samples in the figure show spherical pores with relatively uniform size. According to the design of the synthesis process shown in Figure 1, the pores should be connected, and the holes in the pore walls observed in Figure 4 fit that. EDX analysis proves that the silica particles can be etched away successfully by NaOH solution (see Table S1 in Supplementary Material) as less than 0.5% Si is left on the surface of CuO. 30 measurable pores in the SEM images were measured to get the average pore size of the samples, and it was found that the pore size of the samples were slightly smaller than the diameter of the corresponding silica particle templates used in the synthesis. The mean diameter of CuO-100, CuO-600, CuO-1000 and CuO-2000 are about 82 nm, 574 nm, 937 nm, and 1891 nm, respectively. The smaller diameter is probably caused by shrinkage of the pores during the calcination at 650°C and/or the etching of silica spheres. The pore size of CuO synthesized from 10 nm and 50 nm silica particles were too small to be observed by scanning microscopy, but their pore size can be characterized and calculated by N_2-sorption, by which more comprehensive pore diameter data of the samples can be obtained, including information of the bulk of the pores (adsorption branch) and the pore necks (desorption branch). A closer look inside the pores reveals that the junctions between the spherical pores (i.e. pore necks) are smaller in size than the diameter of the spherical pores themselves. This can be more clearly observed in

330 the CuO SEM images of the larger pores. This is reasonable because the size of the contact
331 surface between the template silica spheres was smaller than the diameter of the spheres
332 themselves. The shape of the pores is a stack of multiple hollow spheres, rather than a cylindrical
333 channel. The SEM images of CuO-100, CuO-600, CuO-1000 and CuO-2000 were only used to
334 measure the diameter of the pore bodies, not the size of the pore necks. To measure the diameter
335 of the pore necks more accurately, mercury intrusion porosimetry was applied.
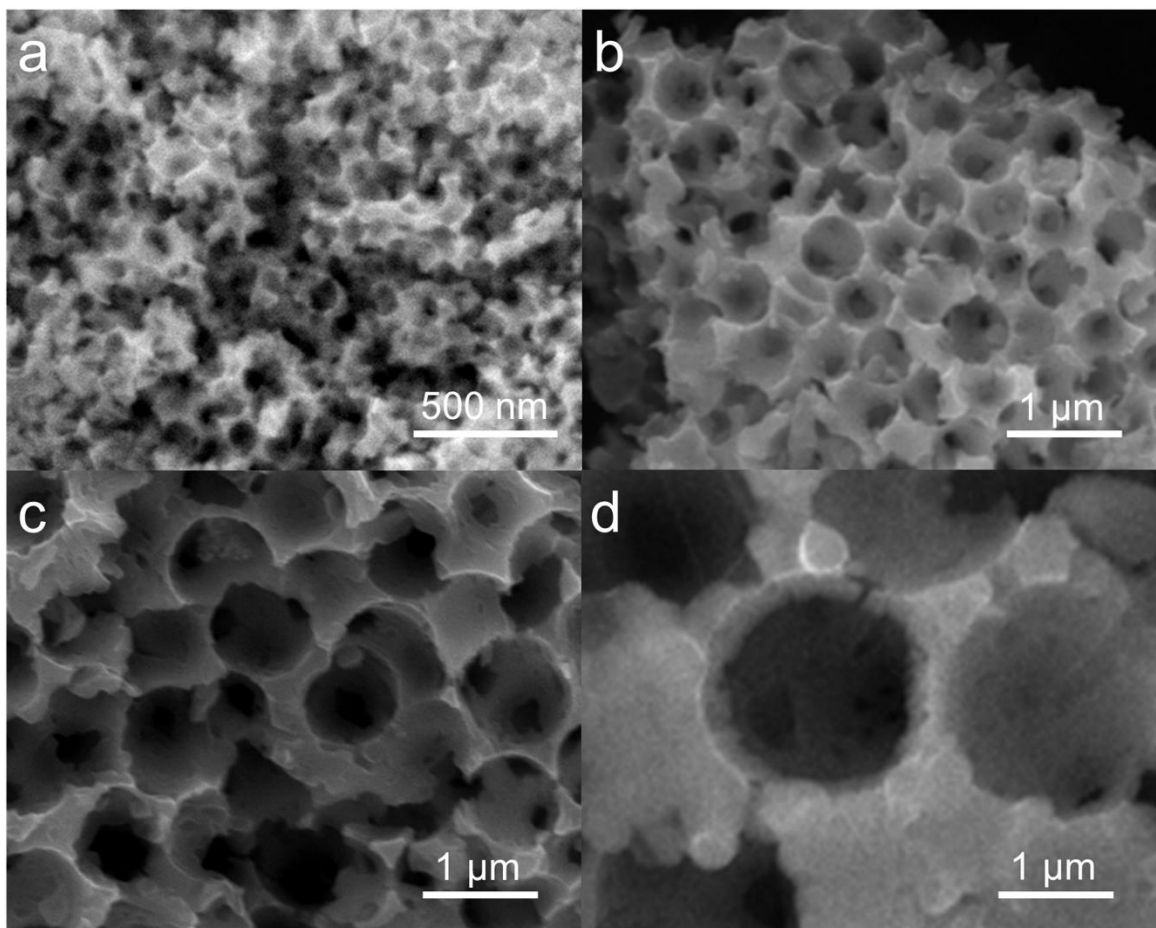

336

337 Figure 4. SEM images of 3D porous CuO. (a) CuO-100 synthesized from silica particles with a diameter of about 100
338 nm. (b) CuO-600 synthesized from silica particles with a diameter of about 600 nm. (c) CuO-1000 synthesized from
339 silica particles with a diameter of about 1 µm. (d) CuO-2000 synthesized from silica particles with a diameter of about
340 2 µm.

341 Figure 5 displays the pore size distribution of the porous copper oxide samples based on N_2-
342 sorption (NLDFT adsorption branch) and mercury intrusion porosimetry. The pore size
343 distribution (calculated by BJH desorption branch) and N_2-soption isotherms of CuO-10 and
344 CuO-50 are shown in Supplementary Material, Figure S2 to obtain more complete information on
345 the pore structure. Since nitrogen sorption and mercury intrusion porosimetery are applicable to
346 different pore size ranges, the CuO-10 and CuO-50 samples were characterized by nitrogen
347 sorption, and the other samples were determined by mercury intrusion porosimetry. Due to the
348 different systematic errors of the two characterization methods, the pore size distribution of
349 samples obtained by different methods cannot be accurately compared, but they are put into the
350 same figure to roughly compare the pore size distributions and get an intuitive impression.
351 Important to note is that, due to the ink-bottle effect, the pore size obtained by mercury intrusion

352 is only the size of pore necks, which will be smaller than the actual bulk pore size (cf. SEM
353 images, Figure 4) of the samples [53,54], while the pore size obtained by N_2-sorption includes
354 both pore neck size (desorption branch, Figure S2) and bulk pore size (adsorption branch, Figure
355 5). The pore size distribution of all samples suggests relatively uniform pores [53]. It is worth
356 mentioning that because the synthesized CuO samples are powders with tens of µm particle size,
357 there is another broad pore size distribution at the micrometer scale in the results of mercury
358 intrusion (as shown in Figure S3), which reflects the size of the inter-particle gaps rather than the
359 bulk pore size [55,56].
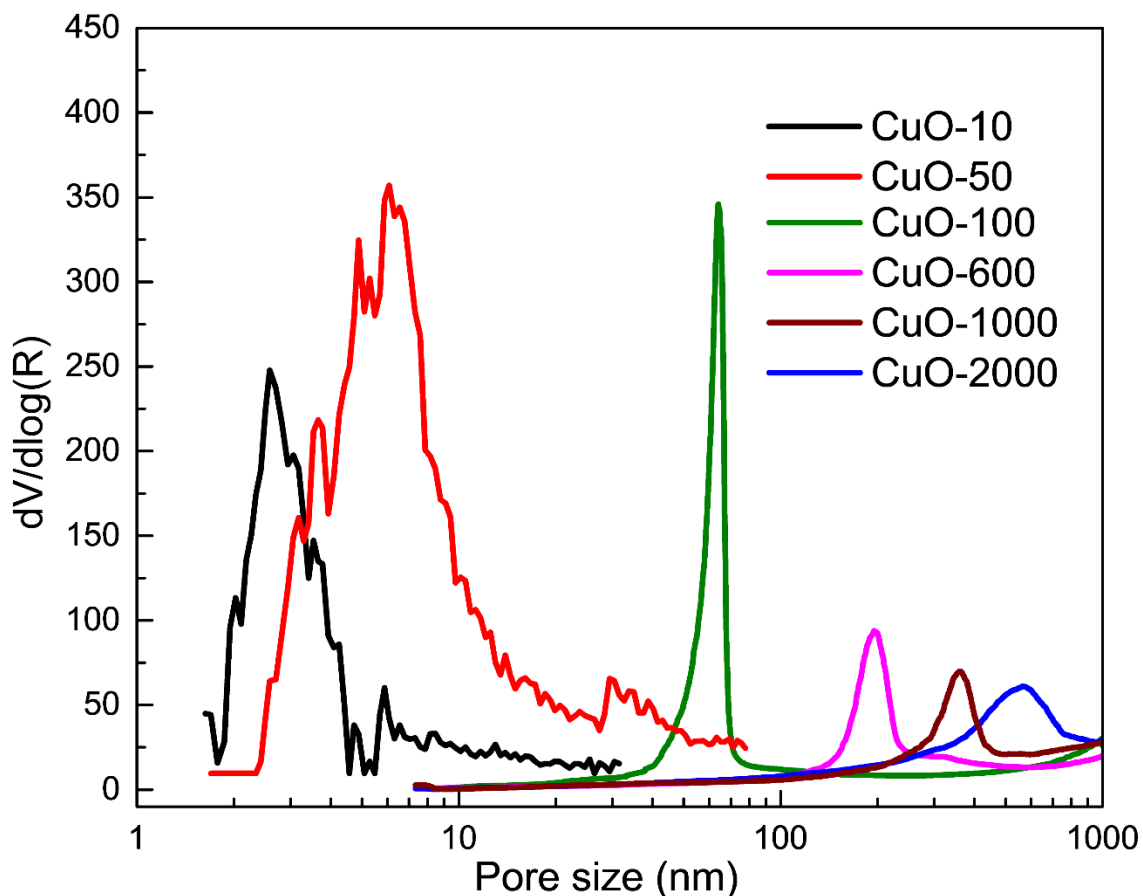
360

361 Figure 5. Pore size distribution of 3D porous CuO samples obtained by N_2-sorption (for CuO-10 and CuO-50) and
362 mercury intrusion (for the other samples).

363   The maxima of the pore size distributions calculated from N_2-sorption and mercury intrusion
364 porosimetry of all CuO samples are listed in Table 1. For CuO-10 and CuO-50, the pore size is
365 much smaller than the diameter of the silica spheres used in the synthesis, which might be caused
366 by shrinkage during thermal treatments [57]. In addition, consistent with the conclusions drawn
367 from the SEM images, the pore neck size of CuO-100, CuO-600, CuO-1000, and CuO-2000
368 measured by mercury intrusion is smaller than the diameter of the silica spheres used in the
369 synthesis. Although the pore size of all porous samples is not equal to the diameter of the silica
370 spheres, it is obvious that there is a positive correlation with it, resulting in an increasing trend
371 with the use of larger silica template particles. Hence, uniform pore catalysts with different pore
372 sizes are indeed successfully prepared over a large pore size span. The apparent surface area
373 determined using the Brunauer–Emmett–Teller (BET) theory by N_2-sorption is also listed in
374 Table 1. Initially, it decreases rapidly with increasing pore size from CuO-10 to CuO-100.

375 However, for the macroporous samples from CuO-100 to CuO-2000, the differences in specific
376 surface area are very small as the pore size changes.

377 Table 1. Pore sizes and specific surface areas of 3D porous CuO samples obtained from N_2-sorption, SEM and mercury
378 intrusion.

| Samples	Bulk pore diameter	Pore neck diameter	Specific surface area	Mean particle diameter[d]	Packing density	Packing density of reduced sample
CuO-10	2.6 nm[a]	/	236 m^2/g	8 μm	1.6 g/mL	1.7 g/mL
CuO-50	6.1 nm[a]	4.3 nm[a]	152 m^2/g	8 μm	1.7 g/mL	1.8 g/mL
CuO-100	82 nm[b]	64.0 nm[c]	8 m^2/g	10 μm	1.7 g/mL	1.7 g/mL
CuO-600	574 nm[b]	195.0 nm[c]	2 m^2/g	9 μm	1.6 g/mL	1.7 g/mL
CuO-1000	937 nm[b]	361.2 nm[c]	2 m^2/g	9 μm	1.6 g/mL	1.7 g/mL
CuO-2000	1891 nm[b]	565.6 nm[c]	1 m^2/g	10 μm	1.7 g/mL	1.8 g/mL

379   [a]Pore size characterized by N_2-sorption, including bulk pore diameter (deduced by NLDFT from the adsorption
380 branch) and pore necks diameter (deduced by BJH from the desorption branch). [b]Bulk pore size measured and
381 calculated by SEM images. [c]Pore size characterized by mercury intrusion, which is considered to only account for the
382 size of the pore necks. [d]The particle distribution is broad (see the SEM images in Figure B.3), and thus the mean value
383 is only present as a rough indication of differences in size between different powders but cannot be used to derive
384 conclusion about e.g. void space due to the broad particle size distribution.

385   In addition, as shown in Figure S4, the porous CuO particles synthesized by the method in this
386 paper are not uniform in shape and particle size. The particle diameters of the porous CuO
387 particles range from ~5 μm to ~40 μm, and the average particle diameters calculated from
388 measurements of more than 50 particles from the SEM images of Figure S4 are summarized in
389 Table 1. As shown in the table, compared with the large differences between the pore diameters
390 (ranging from 2.6 to 1891 nm), the difference in mean particle diameter between the sample
391 particles was relatively small, and the particle diameter did not show an obvious tendency to
392 increase with increasing pore size. The average particle diameter of CuO-10 and CuO-50 was
393 slightly smaller than for the other samples, because they included more small particles around 5
394 μm. Due to the similar mean particle diameters of the samples, their packing densities in the
395 reactor, calculated from the weight of the particles packed in the discharge zone and the volume
396 of the discharge space, as shown in Table 1, did not show significant variations with pore size.
397 Therefore, samples with different pore sizes packed in the DBD reactor are expected to have
398 similar space times. Hence, although the particle size and interparticle void space, as well as the
399 packing density of the particles, could in principle affect the plasma performance and we cannot
400 exclude it, its impact is expected to be less for all packing materials used in this work, compared
401 to the change in pore size, which covers more than three orders of magnitude.

402   The infrared (IR) spectra of the CuO samples with different pore sizes are shown in Figure S5.
403 After flushing with 80 mL/min Ar for 30 min, all CuO samples did not show obvious hydroxyl
404 groups, probably due to the 650 °C calcination during the syntheses. The peaks appearing at
405 around 537 cm^{-1} and 585 cm^{-1} can be attributed to the vibrations of Cu-O. A peak at 835 cm^{-1}
406 could be assigned to the residual traces of silica after the etching, and no other peaks of SiO_2 was

407 observed. A sample of CuO-1000 was characterized by IR again after the DRM, and no
408 significant change on its surface properties was observed after plasma based dry reforming.

409 **3.2. Dry reforming performance of the catalysts with different pore sizes**
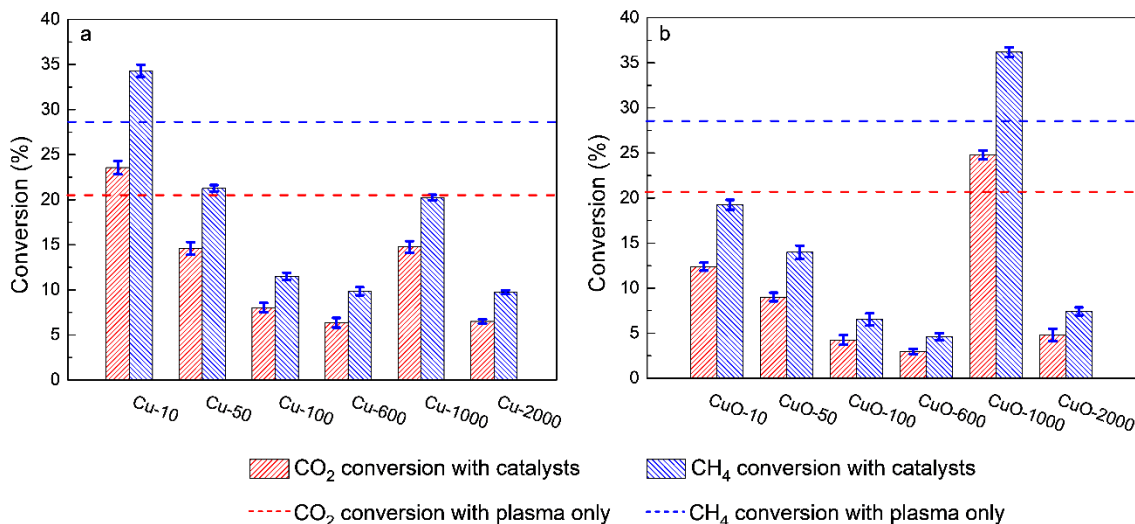
411 Figure 6. Conversion of CH_4 and CO_2 in plasma-catalytic dry reforming, of 3D porous (a) Cu and (b) CuO samples
412 with different pore sizes. The dashed line is the conversion of the empty reactor only with plasma at the same gas flow
413 rate. The error bars were obtained from standard errors based on three repeat experiments.

414   Plasma-catalytic dry reforming tests were performed on porous samples with different pore
415 sizes before and after reduction. Figure S6 shows the results of TPO-TPR-TPO of the samples
416 after reduction. The oxygen consumption of the two TPOs was consistent, indicating that the CuO
417 samples were completely reduced in the tube furnace. The conversions of CH_4 and CO_2 in the
418 plasma-catalytic reaction are shown in Figure 6. The dashed lines in Figure 6 are the CH_4 and
419 CO_2 conversions at the same gas flow in an empty reactor only with plasma. In most cases,
420 similar to the results in the majority of literature on plasma dry reforming, the CH_4 and CO_2
421 conversions for the catalysts were lower than those in the empty reactor at the same flow rate.
422 This is because the positive effects of catalysts are not enough to compensate for their negative
423 effects, such as hindering discharge and reducing space time. However, the best performing
424 samples for a certain pore size in Cu and CuO (i.e. Cu-10 and CuO-1000) exhibited higher
425 conversion than the empty reactor, illustrating the importance of the pore size effect on the
426 plasma catalytic process, and the positive effects of the fully packing catalyst with suitable
427 properties in the plasma catalytic dry reforming can cover its negative effects. There are very
428 similar trends in Figure 6a (reduced copper samples) and Figure 6b (unreduced copper oxide
429 samples). The first trend is that among the samples with pore sizes smaller than Cu-1000 or CuO-
430 1000, the smaller the pore size, the higher the obtained conversion. This seems normal from a
431 thermocatalytic dry reforming point of view, because the smaller pore catalysts have a higher
432 surface area (see specific surface area of the different samples in Table 1) to facilitate the
433 adsorption and catalytic reaction at the surface. In a plasma reaction, however, it is unusual.
434 Previous studies on pore size generally suggested that the high surface area in small pores was
435 ineffective since the smaller the pore size, the fewer electrons in the plasma can propagate into
436 the pores during the discharge [39-41,58-61]. The direct comparison of the performance of
437 catalysts with different pore sizes (Figure 6) shows results that are in contrast to the conclusions
438 drawn from previously reported simulations or experimental studies of plasma propagation within
439 catalyst pores [40,41,59,60]. The results suggest that although electrons may not be able to enter

440   the smaller pores to activate gas molecules and interact with the catalyst surface inside the pores,
441   the smaller pores still have some advantages, which are more important than the fact that plasma
442   cannot enter inside these small pores.

443   First, the advantage of materials with large pores enabling more electrons to enter to react with
444   the surface may not be as great. According to the data shown in Table 1, even if the pore size is
445   large enough that the plasma streamer can propagate directly in it, resulting in the effective
446   surface area of plasma reaction equal to its total surface area, the specific surface area of the
447   catalyst with macropores is so low that it could not bring much benefit to the catalytic reaction.
448   Second, although it is difficult for electrons in the plasma to enter the smaller pores to activate
449   gas molecules due to the prevention of the plasma sheath, radicals or positively charged ions
450   generated in the plasma will not be blocked. These plasma species may still diffuse into the pores,
451   or (in case of the ions) even be accelerated out of the plasma into the pore, and thus react with the
452   catalyst surface [61,62]. The lifetime of the free radicals will determine how deep they can
453   penetrate into the pore. Third, the high roughness of the catalysts with small pores, resulting from
454   the higher number of pores at the surface, causes electric field enhancement in the plasma, which
455   creates more reactive plasma species that can interact with the catalyst. It can also be observed
456   that the plasma power and the average filament charge show a correlation with the conversion of
457   the reactants (we refer to Table 2 later for more details) [42,63-65]. Fourth, The larger external
458   surface area of the catalysts with small pores (again due to a higher number of pores at the
459   surface), may be another reason for their better performance. Fifth, the small crystallite size of
460   catalysts with small pores shown in Figure 3 may also be favorable for the plasma catalytic dry
461   reforming, because the small crystallites have more exposed active sites [66-69]. Sixth, space
462   time may also affect the conversion. As shown in Figure S7, the conversion of CO_2 and CH_4 for
463   two representative samples, i.e., Cu-10 and CuO-1000, is greatly affected by the gas flow rate
464   (which results in different space times). It should be realized that small variation in space time
465   resulting from packing density variation can also affect the performance results to some extent.
466   Moreover, as mentioned before, the CuO-10 and CuO-50 particles had slightly (10–20%) smaller
467   mean particle diameters (8 µm versus 9–10 µm). The void space between the particles and the
468   contact points between particles might be different. This provides a complexity of positive and
469   negative effects of performance, which are mutually interfering and are expected to have an
470   optimum value of particle size [27,28]. However, since the differences in mean particle diameter
471   and packing densities between the samples were small (compared to the 3 orders of magnitude
472   differences in pore sizes) and did not show an obvious trend with pore size, it is difficult to
473   estimate the role of space times, particle sizes and packing densities. Nevertheless, we cannot
474   exclude their effects.

475   In most cases, Cu with the same pore size exhibited better performance than CuO (cf. figure
476   6a and 6b) as metals are the typical active components for dry reforming reactions [42,58]. An
477   exception is observed for the samples synthesized from the 1 µm silica spheres, i.e., the
478   conversion of CuO-1000 is higher than of Cu-1000. These samples are also exceptions to the
479   trend that the smaller the pore size, the better the performance. Indeed, these samples show a
480   higher conversion in plasma-based dry reforming than both the smaller and larger pore size
481   samples, and CuO-1000 even shows the highest conversion among all the unreduced CuO
482   samples. We believe this can be attributed to the electric field enhancement in the pores with
483   diameters close to the plasma Debye length (ca. 600 nm at typical plasma catalysis conditions)
484   [39,40]. This electric field enhancement enables Cu-1000 and CuO-1000 to perform better than
485   the other samples. Since mainly surface discharges occur in DBD plasma packed with materials
486   with relatively low dielectric constant [42,58,70], such as CuO (ε_r = 18.1), the electric field
487   enhancement in this case due to surface charging is stronger than that of Cu-1000. Metals are in
488   this context equivalent to a dielectric with infinite dielectric constant, and thus, the plasma will

489 mainly be characterized by local filamentary microdischarges [42,58,70]. As samples with small
490 pores can provide more and smaller discharge gaps for the local filamentary microdischarges,
491 they are more favorable in Cu samples for the plasma reaction than the electric field enhancement
492 of Cu-1000 [42,70]. The above factors together can explain why CuO-1000 shows the highest
493 conversion of the unreduced CuO samples, while Cu-10 is the best among the reduced Cu
494 samples.

495 Among the other macroporous samples with similar specific surface area, CuO-2000 showed
496 better performance than CuO-600, while the performance of Cu-2000 is similar to that of Cu-600.
497 This might also be because the discharge mode dominated by surface discharges in CuO is more
498 in line with the simulation of plasma propagation in pores [40]. which predicts that a larger pore
499 size allows more electrons to enter. However, in case of metallic materials, the discharge mode
500 (characterized by local filamentary micro-discharges) is different.
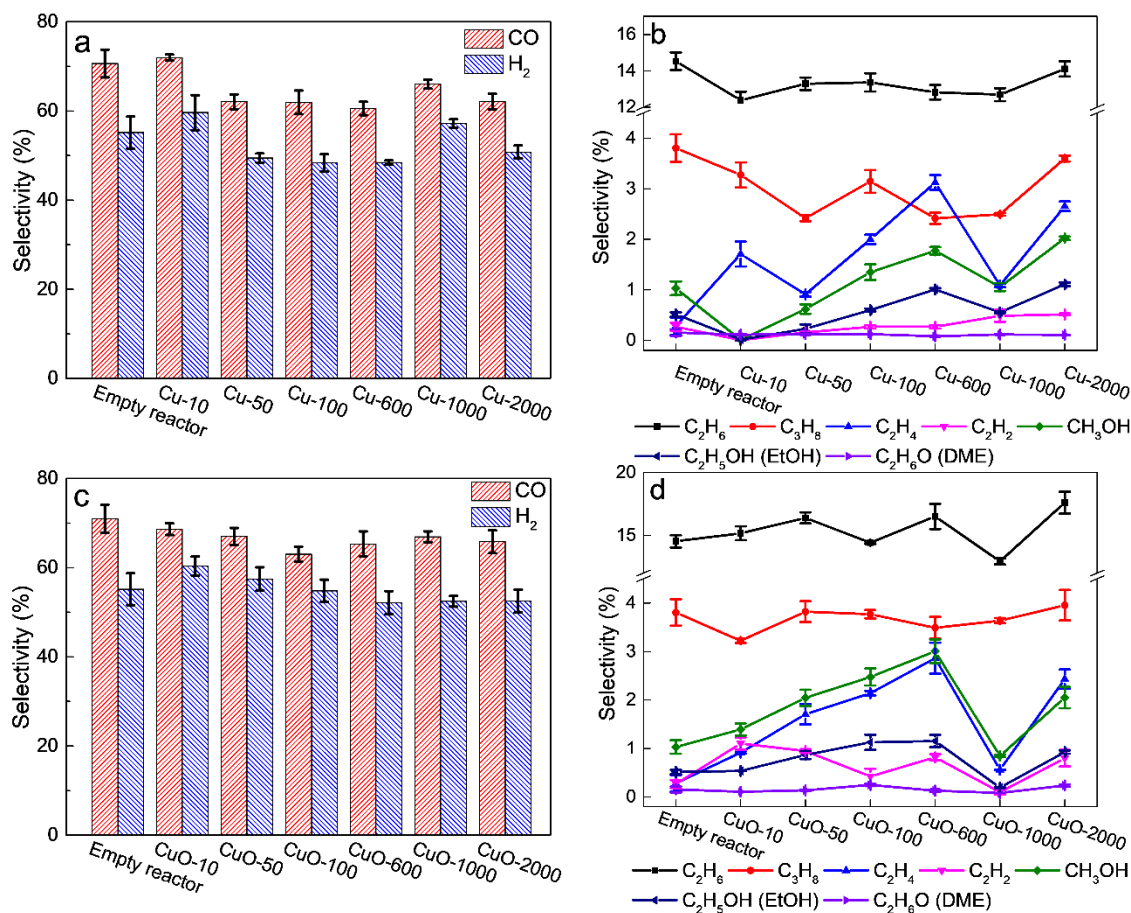
501

502 Figure 7. Product selectivities in plasma-catalytic dry reforming, for CO and H_2 of 3D porous Cu (a) and CuO (c)
503 samples with different pore sizes, and for ethane, propane, ethylene, acetylene, methanol, ethanol and dimethyl ether of
504 3D porous Cu (b) and CuO (d) samples with different pore sizes. The error bars were obtained from standard errors
505 based on three repeats.

506 The selectivities of the main components formed in plasma-catalytic dry reforming with the
507 various 3D porous samples with different pore sizes are plotted in Figure 7. The carbon and
508 hydrogen mass balance (shown in Figure S8) is not entirely 100%. Therefore, there might still be
509 a few possible liquid products and carbon deposits attached to the catalyst and the reactor, as well

510 as the presence of other gaseous products that were not calibrated in the gas chromatograph,
511 which cannot be counted. As shown in Figure 7a and Figure 7c, syngas is the predominant
512 product in all experiments, and the CO selectivity is always higher than that of H_2. When
513 comparing the samples with different pore sizes, some products do not differ significantly in
514 selectivity, while others do. Interestingly, the difference in selectivity appears to correlate with
515 the conversion of the reactants. A rough trend seems to be that samples exhibiting higher CH_4 and
516 CO_2 conversions also have higher syngas (CO and H_2) selectivities, but lower selectivities for
517 some unsaturated hydrocarbons and oxygenated organics, such as ethylene, methanol, and ethanol.
518 The selectivity decrease is most striking for the Cu-1000 and CuO-1000 samples, and may be
519 caused by the enhanced electric field in the samples, causing a higher conversion due to the
520 higher energy input, and apparently a lower selectivity to these unsaturated hydrocarbons and
521 oxygenates, in line with literature [33,45]. The empty reactor had higher plasma power (see Table
522 2 below) due to the absence of packing material which may hinder the discharge, also following
523 the above trend, which exhibited a relatively high syngas selectivity and a low unsaturated
524 hydrocarbon and oxygenates selectivity. Besides the electric field enhancement, the reaction of
525 radicals within the pores is another factor that might affect the selectivity [61,62]. The trends in
526 selectivity for the various products are different, indicating a different impact of the pore size on
527 the reaction paths of the radicals. For example, the selectivity towards acetylene is low in CuO-
528 1000 but relatively high in CuO-10, although both of them show a high conversion of CO_2 and
529 CH_4. Since CO is the predominant carbon-containing product, the carbon balance shown in
530 Figure S8 has a similar trend to the selectivity of CO. For example, among the copper samples,
531 Cu-10 also has the highest sum of detectable carbon-containing products selectivities. However,
532 the carbon balance of CuO-1000 is lower than that of other samples, although its CO selectivity is
533 similar or even slightly higher than other samples. This indicates that more carbon deposits or
534 other products not calibrated in the GC were generated during the dry reforming of this sample.

535 In order to study the stability of dry reforming performance and possible carbon deposition on
536 the samples, long-time plasma DRM tests and TGA measurements were performed. As shown in
537 Figure S9, the performance of Cu-10 decreased slightly (1%–2%) after 12 h of testing, while the
538 conversion of CH_4 and CO_2 of CuO-1000 did not change significantly (< 1%). Figure S10 shows
539 the TGA data of CuO-1000 and Cu-10 after 12 h plasma dry reforming. The used CuO-1000 has
540 a small weight loss (~ 0.1%) when heated to 800 °C in 80 mL/min of O_2, indicating that there is
541 little carbon deposition on its surface and it was not reduced by H_2 and CO products in plasma
542 dry reforming, which may be due to the relatively low input energy in this study. The TGA data
543 of the used Cu-10 were compared with that of fresh Cu-10, since the weight loss was covered by
544 the weight increase caused by the oxidation of Cu. The weight difference after heating to 800°C
545 between the fresh Cu-10 and used Cu-10 was about 4.5%, which could be attributed to the carbon
546 deposition from the 12 h plasma dry reforming, and this is also in line with its slightly reduced
547 performance. In addition, as shown in Figure S11, the reducibility of CuO-1000 did not change
548 after the DRM test.

549 The electrical signals of the plasma experiments were recorded and collected by an
550 oscilloscope. As seen in Table 2, 26–28 kV peak-to-peak voltage (U_{pp}) was applied to achieve a
551 constant 50 W supplied power. However, depending on some factors, such as the structure and
552 dielectric constant of the packing samples, at the same supplied power, the distribution, number
553 and intensity of the discharges are different, resulting in different plasma powers. The portion of
554 the supplied power that is not converted to plasma power is lost in the circuit as heat or returned
555 to the source as reactive power. A higher plasma power, such as for the Cu-10, CuO-10, and
556 CuO-1000 samples, means higher energy input, which produces a more reactive plasma, leading
557 to their higher conversion. The higher plasma power in the empty reactor illustrates the hindering
558 effect of the catalyst in the discharge, which should be one of the reasons why the conversion of

most samples is lower than that in the empty reactor. The average number of micro-discharges per period is counted by the number of peaks in the normalized current profile after excluding signal noise. It may not be the exact number of micro-discharges, but subject to some system errors, as some discharges may coincide, or some may be too small and therefore are excluded as signal noise. By dividing the transferred charge by the number of micro-discharges in the same period, we obtain the average filament charge, which is a measure for the average strength of the discharge. Both a larger number of micro-discharges and more powerful discharges can have a positive effect on the conversion of plasma-based dry reforming. However, it is difficult for both to achieve relatively high values in the same reaction, since the catalyst pore size did not show a significant effect on the displaced charge. The displaced charge of the empty reactor could not be obtaine due to the limited measurement range of the PC-connected oscilloscope and the unstable discharge in the empty reactor. As shown in Table 2, a higher average filament charge often corresponds with fewer discharges, and exhibits higher conversion, cfr. Figure 6. Therefore, our results suggest that the strength of the discharges has a larger effect on the conversion of plasma-based dry reforming than the number of micro-discharges.

However, most copper samples showed lower plasma power and discharge intensity than copper oxide with the same structure, despite they had a higher conversion of CO_2 and CH_4. The packing of the porous Cu powders in the reactor made some conductive particles to be directly connected to the grounded inner electrode to form an equipotential, which may cause most of the discharge to occur in the small gaps between the outermost particles (probably at the same potential as the electrode) and the dielectric barrier, and less point-to-point micro-discharges in the gaps between the other powders in the gap [42,58,70]. Although the reduced Cu has a negative impact on the discharge, they showed better performance in most cases than the CuO samples with higher plasma power and more produced radicals and ions, which might be due to its better catalytic activity for dry reforming. Figure S12 shows the energy yields of the different samples, which exhibit the sample performance after normalizing for the difference in discharge power. The trend of EY variation with pore size is similar to that of conversion, further confirming the effect of pore size of the samples on the dry reforming performance. Since the discharge power of the Cu samples is always lower than that of the CuO samples, the performance advantage of Cu over CuO, shown by the EY, is larger than that shown by the conversion (except for Cu-1000 and CuO-1000). Since one of the reasons why the empty reactor has a higher conversion than most samples is its high discharge power, after excluding the influence of discharge power, two more samples, i.e., Cu-50 and Cu-1000, show better performance than the empty reactor, based on the EY.

593 Table 2. Electrical characterization data measured and calculated from the recorded signals of the oscilloscope of the
594 DRM experiments with the samples of different pore sizes.

Samples	U_{PP} (kV)	Power supplied (W)	Plasma power (W)	Displaced charge (nC)	Number of micro-discharges (a.u./T)	Average filament charge (nC/disch.)
Empty reactor	25.9	50.5	27.8	/	176	/
Cu-10	26.3	50.5	19.5	558	141	4.2
Cu-50	28.3	50.2	15.7	596	137	3.8
Cu-100	26.7	50.2	16.5	529	168	3.3
Cu-600	27.3	50.2	16.5	561	154	3.2
Cu-1000	28.0	50.1	15.7	488	139	4.1
Cu-2000	26.6	50.3	17.2	562	165	3.8
CuO-10	26.9	50.4	20.1	547	138	4.0
CuO-50	26.7	49.9	19.3	557	156	3.6
CuO-100	26.4	50.3	19.7	671	134	5.0
CuO-600	26.4	50.3	19.2	665	155	4.3
CuO-1000	26.0	50.6	24.4	608	85	7.2
CuO-2000	26.8	50.5	19.5	589	151	3.9

595

4. Conclusion

597   In this study, we investigated the effect of catalyst pore size on plasma-based dry reforming.
598 The samples evaluated in this study were 3D porous Cu or CuO, synthesized from uniform silica
599 particles in the range of 10 nm to 2 μm used as templates. Since the samples have similar pore
600 structure, and consist of the same single chemistry without the interference of a support material,
601 the plasma results can clearly show the influence of the catalyst pores in the plasma-based dry
602 reforming.

603   Based on the conclusions drawn from previous simulation studies, we would expect that the
604 larger the pore size, the better the catalyst performance, and the best results would be obtained for
605 catalyst pore sizes above the plasma Debye length (hundreds of nanometers at typical plasma
606 catalysis conditions [39,40]). That is because pores larger than the Debye length allow the plasma
607 streamer to penetrate inside the catalyst pores and thus generate a larger contact area between
608 plasma and catalyst surface for chemical reactions. However, our results do not reveal that the
609 larger catalyst pore size is more favorable for the plasma reaction, but they show the opposite
610 trend in most cases, with the exception of CuO-1000 (and Cu-1000 to some extent as well). This
611 suggests that even when the electrons cannot enter the catalyst pores, because they are smaller
612 than the Debye length, these pores can still be reached by radicals formed in the plasma, and ions
613 can even be attracted into them due to the electric field, and these radicals and ions can give rise
614 to the plasma-catalytic reactions. Among the reduced Cu samples, Cu-10 showed the highest
615 conversion of CH_4 and CO_2, while among the CuO samples, CuO-1000 showed the highest
616 conversion. We attribute the latter to the electric field enhancement, as predicted by modeling, as
617 this pore size is close to the Debye length. The conversions of CH_4 and CO_2 of Cu-10 and CuO-
618 1000 are higher than those of the empty reactor, indicating that the fully packing catalyst does not
619 necessarily have a negative effect on the conversion as in the literature, and as long as it has a

620 suitable structure, the conversions of of CH_4 and CO_2 can be improved. Furthermore, a rough
621 trend indicates that the higher the conversion of CH_4 and CO_2, the generally higher is the
622 selectivity of syngas among the various products, and the lower is the selectivity of some
623 unsaturated hydrocarbons and oxygenated organics. Finally, from the correlation with the
624 electrical characteristics, we can conclude that the strength of the micro-discharges has an
625 important effect on the conversion of CH_4 and CO_2 and the selectivity of the products, although
626 there is no perfect correlation.

627 In the 3D porous samples synthesized by the template method, the thickness of the pore wall
628 varies with the pore size, resulting in changes in the crystallite size of the components. Samples
629 with larger pore sizes have larger crystallite size, which is detrimental to the conversion of dry
630 reforming [66-69]. The difference in specific surface area for samples with pore sizes smaller
631 than 100 nm and samples with larger pores is two orders of magnitude. Therefore, even if the
632 plasma streamers can propagate into the large pores and react with the entire surface of the
633 sample, which is not possible for the pores smaller than the Debye length, the total contact area
634 with plasma will not rise a lot, and thus, it will not bring much improvement. On the other hand,
635 even if plasma streamers cannot propagate in the smaller pores, as mentioned above, radicals or
636 positively charged ions can still diffuse into these catalysts, and the latter even be attracted into it,
637 and the effective contact area of these radicals and ions in small pores is much larger than for
638 catalysts with larger pores.

639 In summary, we demonstrated that catalysts with smaller pores perform generally better for
640 plasma-based dry reforming, but there are exceptions depending on the properties of the materials.
641 The possible electric field enhancement due to surface charging in the large pores of a certain
642 pore size can greatly improve the reaction efficiency. This enhancement effect is strong for CuO,
643 which is characterized by a relatively small dielectric constant, while it is weak for metallic
644 catalytically active components. Therefore, in future research of catalysts for plasma reactions,
645 macroporous supports with specific pore size (possibly several hundreds of nanometers) and
646 metal active components with micropores (or the combination of both) are two potential feasible
647 directions. This is not only for dry reforming, but could also be valid for more plasma-catalytic
648 processes.

Acknowledgements

Declaration of competing interest

657 The authors declare no known competing financial interest or personal relationships that could
658 inappropriately influence this work.

Appendix A. Supplementary Material

660 Supplementary data associated with this article can be found in the online version.

References

661

662 [1] A. Bogaerts, X. Tu, J.C. Whitehead, G. Centi, L. Lefferts, O. Guaitella, F. Azzolina-Jury, H.-H.
663 Kim, A.B. Murphy, W.F. Schneider, T. Nozaki, J.C. Hicks, A. Rousseau, F. Thevenet, A. Khacef, M.
664 Carreon, The 2020 plasma catalysis roadmap, J. Phys. D Appl. Phys. 53 (2020) 443001.
665 https://doi.org/10.1088/1361-6463/ab9048.

666 [2] Y. Yi, J. Zhou, H. Guo, J. Zhao, J. Su, L. Wang, X. Wang, W. Gong, Safe Direct Synthesis of High
667 Purity H_2O_2 through a H_2/O_2 Plasma Reaction, Angew. Chem. Int. Ed. 52 (2013) 8446-8449.
668 https://doi.org/https://doi.org/10.1002/anie.201304134.

669 [3] Y. Yi, S. Li, Z. Cui, Y. Hao, Y. Zhang, L. Wang, P. Liu, X. Tu, X. Xu, H. Guo, A. Bogaerts, Selective
670 oxidation of CH_4 to CH_3OH through plasma catalysis: Insights from catalyst characterization and
671 chemical kinetics modelling, Appl. Catal. B Environ. 296 (2021) 120384.
672 https://doi.org/10.1016/j.apcatb.2021.120384.

673 [4] Y. Song, E. Ozdemir, S. Ramesh, A. Adishev, S. Subramanian, A. Harale, M. Albuali, A. Fadhel
674 Bandar, A. Jamal, D. Moon, H. Choi Sun, T. Yavuz Cafer, Dry reforming of methane by stable Ni–
675 Mo nanocatalysts on single-crystalline MgO, Science 367 (2020) 777-781.
676 https://doi.org/10.1126/science.aav2412.

677 [5] C. Wang, Y. Wang, M. Chen, D. Liang, Z. Yang, W. Cheng, Z. Tang, J. Wang, H. Zhang, Recent
678 advances during CH_4 dry reforming for syngas production: A mini review, Int. J. Hydrogen Energy
679 46 (2021) 5852-5874. https://doi.org/10.1016/j.ijhydene.2020.10.240.

680 [6] L. Zhou, J.M.P. Martirez, J. Finzel, C. Zhang, D.F. Swearer, S. Tian, H. Robatjazi, M. Lou, L.
681 Dong, L. Henderson, P. Christopher, E.A. Carter, P. Nordlander, N.J. Halas, Light-driven methane
682 dry reforming with single atomic site antenna-reactor plasmonic photocatalysts, Nat. Energy 5
683 (2020) 61-70. https://doi.org/10.1038/s41560-019-0517-9.

684 [7] C. Palmer, D.C. Upham, S. Smart, M.J. Gordon, H. Metiu, E.W. McFarland, Dry reforming of
685 methane catalysed by molten metal alloys, Nat. Catal. 3 (2020) 83-89.
686 https://doi.org/10.1038/s41929-019-0416-2.

687 [8] H.U. Hambali, A.A. Jalil, A.A. Abdulrasheed, T.J. Siang, A.H.K. Owgi, F.F.A. Aziz, CO_2 reforming
688 of methane over Ta-promoted Ni/ZSM-5 fibre-like catalyst: Insights on deactivation behavior
689 and optimization using response surface methodology (RSM), Chem. Eng. Sci. 231 (2021) 116320.
690 https://doi.org/10.1016/j.ces.2020.116320.

691 [9] L.C. Buelens, V.V. Galvita, H. Poelman, C. Detavernier, G.B. Marin, Super-dry reforming of
692 methane intensifies CO_2 utilization via Le Chatelie's principle, Science 354 (2016) 449-452.
693 https://doi.org/doi:10.1126/science.aah7161.

694 [10] M. Usman, W.M.A. Wan Daud, H.F. Abbas, Dry reforming of methane: Influence of process
695 parameters—A review, Renewable and Sustainable Energy Reviews 45 (2015) 710-744.
696 https://doi.org/10.1016/j.rser.2015.02.026.

697 [11] G. Zhang, J. Liu, Y. Xu, Y. Sun, A review of CH_4-CO_2 reforming to synthesis gas over Ni-based
698 catalysts in recent years (2010–2017), Int. J. Hydrogen Energy 43 (2018) 15030-15054.
699 https://doi.org/10.1016/j.ijhydene.2018.06.091.

700 [12] N.A.K. Aramouni, J.G. Touma, B.A. Tarboush, J. Zeaiter, M.N. Ahmad, Catalyst design for dry
701 reforming of methane: Analysis review, Renewable and Sustainable Energy Reviews 82 (2018)
702 2570-2585. https://doi.org/10.1016/j.rser.2017.09.076.

703 [13] R.S. Abiev, D.A. Sladkovskiy, K.V. Semikin, D.Y. Murzin, E.V. Rebrov, Non-Thermal Plasma for
704 Process and Energy Intensification in Dry Reforming of Methane, Catalysts 10 (2020) 1358.
705 https://doi.org/10.3390/catal10111358.

706 [14] C. Shi, S. Wang, X. Ge, S. Deng, B. Chen, J. Shen, A review of different catalytic systems for
707 dry reforming of methane: Conventional catalysis-alone and plasma-catalytic system, J. CO2
708 Utilzation 46 (2021) 101462. https://doi.org/10.1016/j.jcou.2021.101462.

709 [15] Z. Li, Q. Lin, M. Li, J. Cao, F. Liu, H. Pan, Z. Wang, S. Kawi, Recent advances in process and
710 catalyst for CO_2 reforming of methane, Renewable and Sustainable Energy Reviews 134 (2020)
711 110312. https://doi.org/10.1016/j.rser.2020.110312.

712 [16] R. Snoeckx, A. Bogaerts, Plasma technology – a novel solution for CO_2 conversion?, Chem.
713 Soc. Rev. 46 (2017) 5805-5863. https://doi.org/10.1039/C6CS00066E.

714 [17] B.S. Patil, N. Cherkasov, J. Lang, A.O. Ibhadon, V. Hessel, Q. Wang, Low temperature
715 plasma-catalytic NO_x synthesis in a packed DBD reactor: Effect of support materials and
716 supported active metal oxides, Appl. Catal. B Environ. 194 (2016) 123-133.
717 https://doi.org/10.1016/j.apcatb.2016.04.055.

718 [18] L. Wang, Y. Yi, C. Wu, H. Guo, X. Tu, One-Step Reforming of CO_2 and CH_4 into High-Value
719 Liquid Chemicals and Fuels at Room Temperature by Plasma-Driven Catalysis, Angew. Chem. Int.
720 Ed. 56 (2017) 13679-13683. https://doi.org/https://doi.org/10.1002/anie.201707131.

721 [19] Y. Uytdenhouwen, K.M. Bal, E.C. Neyts, V. Meynen, P. Cool, A. Bogaerts, On the kinetics and
722 equilibria of plasma-based dry reforming of methane, Chem. Eng. J. 405 (2021) 126630.
723 https://doi.org/https://doi.org/10.1016/j.cej.2020.126630.

724 [20] X. Tu, J.C. Whitehead, Plasma dry reforming of methane in an atmospheric pressure AC
725 gliding arc discharge: Co-generation of syngas and carbon nanomaterials, Int. J. Hydrogen
726 Energy 39 (2014) 9658-9669. https://doi.org/https://doi.org/10.1016/j.ijhydene.2014.04.073.

727 [21] Y. Yi, C. Xu, L. Wang, J. Yu, Q. Zhu, S. Sun, X. Tu, C. Meng, J. Zhang, H. Guo, Selectivity control
728 of H_2/O_2 plasma reaction for direct synthesis of high purity H_2O_2 with desired concentration,
729 Chem. Eng. J. 313 (2017) 37-46. https://doi.org/https://doi.org/10.1016/j.cej.2016.12.043.

730 [22] A.H. Khoja, M. Tahir, N.A.S. Amin, Dry reforming of methane using different dielectric
731 materials and DBD plasma reactor configurations, Energy Convers. Manage. 144 (2017) 262-274.
732 https://doi.org/https://doi.org/10.1016/j.enconman.2017.04.057.

733   [23] Y. Uytdenhouwen, J. Hereijgers, T. Breugelmans, P. Cool, A. Bogaerts, How gas flow design
734   can influence the performance of a DBD plasma reactor for dry reforming of methane, Chem.
735   Eng. J. 405 (2021) 126618. https://doi.org/https://doi.org/10.1016/j.cej.2020.126618.

736   [24] F. Zhu, H. Zhang, X. Yan, J. Yan, M. Ni, X. Li, X. Tu, Plasma-catalytic reforming of CO_2-rich
737   biogas over Ni/γ-Al_2O_3 catalysts in a rotating gliding arc reactor, Fuel 199 (2017) 430-437.
738   https://doi.org/https://doi.org/10.1016/j.fuel.2017.02.082.

739   [25] M.-w. Li, G.-h. Xu, Y.-l. Tian, L. Chen, H.-f. Fu, Carbon Dioxide Reforming of Methane Using
740   DC Corona Discharge Plasma Reaction, J. Phys. Chem. A 108 (2004) 1687-1693.
741   https://doi.org/10.1021/jp037008q.

742   [26] Y. Yi, X. Wang, A. Jafarzadeh, L. Wang, P. Liu, B. He, J. Yan, R. Zhang, H. Zhang, X. Liu, H. Guo,
743   E.C. Neyts, A. Bogaerts, Plasma-Catalytic Ammonia Reforming of Methane over Cu-Based
744   Catalysts for the Production of HCN and H_2 at Reduced Temperature, ACS Catalysis 11 (2021)
745   1765-1773. https://doi.org/10.1021/acscatal.0c04940.

746   [27] I. Michielsen, Y. Uytdenhouwen, J. Pype, B. Michielsen, J. Mertens, F. Reniers, V. Meynen, A.
747   Bogaerts, CO_2 dissociation in a packed bed DBD reactor: First steps towards a better
748   understanding of plasma catalysis, Chem. Eng. J. 326 (2017) 477-488.
749   https://doi.org/https://doi.org/10.1016/j.cej.2017.05.177.

750   [28] Y. Uytdenhouwen, S. Van Alphen, I. Michielsen, V. Meynen, P. Cool, A. Bogaerts, A packed-
751   bed DBD micro plasma reactor for CO_2 dissociation: Does size matter?, Chem. Eng. J. 348 (2018)
752   557-568. https://doi.org/https://doi.org/10.1016/j.cej.2018.04.210.

753   [29] Y. Uytdenhouwen, K.M. Bal, I. Michielsen, E.C. Neyts, V. Meynen, P. Cool, A. Bogaerts, How
754   process parameters and packing materials tune chemical equilibrium and kinetics in plasma-
755   based CO_2 conversion, Chem. Eng. J. 372 (2019) 1253-1264.
756   https://doi.org/https://doi.org/10.1016/j.cej.2019.05.008.

757   [30] B. Wang, M. Mikhail, S. Cavadias, M. Tatoulian, P. Da Costa, S. Ognier, Improvement of the
758   activity of CO_2 methanation in a hybrid plasma-catalytic process in varying catalyst particle size
759   or under pressure, J. CO2 Utilzation 46 (2021) 101471.
760   https://doi.org/https://doi.org/10.1016/j.jcou.2021.101471.

761   [31] R. Vakili, R. Gholami, C.E. Stere, S. Chansai, H. Chen, S.M. Holmes, Y. Jiao, C. Hardacre, X.
762   Fan, Plasma-assisted catalytic dry reforming of methane (DRM) over metal-organic frameworks
763   (MOFs)-based catalysts, Appl. Catal. B Environ. 260 (2020) 118195.
764   https://doi.org/https://doi.org/10.1016/j.apcatb.2019.118195.

765   [32] Y. Zeng, X. Zhu, D. Mei, B. Ashford, X. Tu, Plasma-catalytic dry reforming of methane over γ-
766   Al_2O_3 supported metal catalysts, Catal. Today 256 (2015) 80-87.
767   https://doi.org/https://doi.org/10.1016/j.cattod.2015.02.007.

768   [33] X. Tu, H.J. Gallon, M.V. Twigg, P.A. Gorry, J.C. Whitehead, Dry reforming of methane over a
769   Ni/Al_2O_3 catalyst in a coaxial dielectric barrier discharge reactor, J. Phys. D Appl. Phys. 44 (2011)
770   274007. https://doi.org/10.1088/0022-3727/44/27/274007.

771 [34] H.K. Song, J.-W. Choi, S.H. Yue, H. Lee, B.-K. Na, Synthesis gas production via dielectric
772 barrier discharge over Ni/γ-Al$_2$O$_3$ catalyst, Catal. Today 89 (2004) 27-33.
773 https://doi.org/https://doi.org/10.1016/j.cattod.2003.11.009.

774 [35] J. Sentek, K. Krawczyk, M. Młotek, M. Kalczewska, T. Kroker, T. Kolb, A. Schenk, K.-H.
775 Gericke, K. Schmidt-Szałowski, Plasma-catalytic methane conversion with carbon dioxide in
776 dielectric barrier discharges, Appl. Catal. B Environ. 94 (2010) 19-26.
777 https://doi.org/https://doi.org/10.1016/j.apcatb.2009.10.016.

778 [36] I. Michielsen, Y. Uytdenhouwen, A. Bogaerts, V. Meynen, Altering Conversion and Product
779 Selectivity of Dry Reforming of Methane in a Dielectric Barrier Discharge by Changing the
780 Dielectric Packing Material, Catalysts 9 (2019). https://doi.org/10.3390/catal9010051.

781 [37] J.A. Andersen, J.M. Christensen, M. Østberg, A. Bogaerts, A.D. Jensen, Plasma-catalytic dry
782 reforming of methane: Screening of catalytic materials in a coaxial packed-bed DBD reactor,
783 Chem. Eng. J. 397 (2020) 125519. https://doi.org/https://doi.org/10.1016/j.cej.2020.125519.

784 [38] X. Tu, J.C. Whitehead, Plasma-catalytic dry reforming of methane in an atmospheric
785 dielectric barrier discharge: Understanding the synergistic effect at low temperature, Appl. Catal.
786 B Environ. 125 (2012) 439-448. https://doi.org/https://doi.org/10.1016/j.apcatb.2012.06.006.

787 [39] Q.-Z. Zhang, A. Bogaerts, Plasma streamer propagation in structured catalysts, Plasma
788 Sources Sci. Technol. 27 (2018) 105013. https://doi.org/10.1088/1361-6595/aae430.

789 [40] Q.-Z. Zhang, A. Bogaerts, Propagation of a plasma streamer in catalyst pores, Plasma
790 Sources Sci. Technol. 27 (2018) 035009. https://doi.org/10.1088/1361-6595/aab47a.

791 [41] Y.-R. Zhang, K. Van Laer, E.C. Neyts, A. Bogaerts, Can plasma be formed in catalyst pores? A
792 modeling investigation, Appl. Catal. B Environ. 185 (2016) 56-67.
793 https://doi.org/https://doi.org/10.1016/j.apcatb.2015.12.009.

794 [42] Q.-Z. Zhang, W.-Z. Wang, A. Bogaerts, Importance of surface charging during plasma
795 streamer propagation in catalyst pores, Plasma Sources Sci. Technol. 27 (2018) 065009.
796 https://doi.org/10.1088/1361-6595/aaca6d.

797 [43] X. Zheng, S. Tan, L. Dong, S. Li, H. Chen, LaNiO$_3$@SiO$_2$ core–shell nano-particles for the dry
798 reforming of CH$_4$ in the dielectric barrier discharge plasma, Int. J. Hydrogen Energy 39 (2014)
799 11360-11367. https://doi.org/https://doi.org/10.1016/j.ijhydene.2014.05.083.

800 [44] D. Ray, D. Nepak, T. Vinodkumar, C. Subrahmanyam, g-C$_3$N$_4$ promoted DBD plasma assisted
801 dry reforming of methane, Energy 183 (2019) 630-638.
802 https://doi.org/https://doi.org/10.1016/j.energy.2019.06.147.

803 [45] D. Ray, P.M.K. Reddy, C. Subrahmanyam, Ni-Mn/γ-Al$_2$O$_3$ assisted plasma dry reforming of
804 methane, Catal. Today 309 (2018) 212-218.
805 https://doi.org/https://doi.org/10.1016/j.cattod.2017.07.003.

806 [46] D. Ray, D. Nepak, S. Janampelli, P. Goshal, C. Subrahmanyam, Dry Reforming of Methane in
807 DBD Plasma over Ni-Based Catalysts: Influence of Process Conditions and Support on

808 Performance and Durability, Energy Technol. 7 (2019) 1801008.
809 https://doi.org/https://doi.org/10.1002/ente.201801008.

810 [47] X. Gao, Z. Lin, T. Li, L. Huang, J. Zhang, S. Askari, N. Dewangan, A. Jangam, S. Kawi, Recent
811 Developments in Dielectric Barrier Discharge Plasma-Assisted Catalytic Dry Reforming of
812 Methane over Ni-Based Catalysts, Catalysts 11 (2021). https://doi.org/10.3390/catal11040455.

813 [48] Q. Xie, S. Zhuge, X. Song, M. Lu, F. Yu, R. Ruan, Y. Nie, Non-thermal atmospheric plasma
814 synthesis of ammonia in a DBD reactor packed with various catalysts, J. Phys. D Appl. Phys. 53
815 (2019) 064002. https://doi.org/10.1088/1361-6463/ab57e5.

816 [49] A.H. Khoja, M. Tahir, N.A.S. Amin, Recent developments in non-thermal catalytic DBD
817 plasma reactor for dry reforming of methane, Energy Convers. Manage. 183 (2019) 529-560.
818 https://doi.org/https://doi.org/10.1016/j.enconman.2018.12.112.

819 [50] J. Wang, K. Zhang, S. Kavak, S. Bals, V. Meynen, Modifying the Stöber Process: Is the Organic
820 Solvent Indispensable?, Chemistry – A European Journal n/a (2022).
821 https://doi.org/https://doi.org/10.1002/chem.202202670.

822 [51] J. Van Turnhout, D. Aceto, A. Travert, P. Bazin, F. Thibault-Starzyk, A. Bogaerts, F. Azzolina-
823 Jury, Observation of surface species in plasma-catalytic dry reforming of methane in a novel
824 atmospheric pressure dielectric barrier discharge in situ IR cell, Catalysis Science & Technology
825 12 (2022) 6676-6686. https://doi.org/10.1039/D2CY00311B.

826 [52] N. Pinhão, A. Moura, J.B. Branco, J. Neves, Influence of gas expansion on process
827 parameters in non-thermal plasma plug-flow reactors: A study applied to dry reforming of
828 methane, Int. J. Hydrogen Energy 41 (2016) 9245-9255.
829 https://doi.org/https://doi.org/10.1016/j.ijhydene.2016.04.148.

830 [53] Y. Zhang, B. Yang, Z. Yang, G. Ye, Ink-bottle Effect and Pore Size Distribution of Cementitious
831 Materials Identified by Pressurization–Depressurization Cycling Mercury Intrusion Porosimetry,
832 Materials 12 (2019). https://doi.org/10.3390/ma12091454.

833 [54] F. Moro, H. Böhni, Ink-Bottle Effect in Mercury Intrusion Porosimetry of Cement-Based
834 Materials, J. Colloid Interface Sci. 246 (2002) 135-149.
835 https://doi.org/https://doi.org/10.1006/jcis.2001.7962.

836 [55] R.P. Mayer, R.A. Stowe, Mercury porosimetry—breakthrough pressure for penetration
837 between packed spheres, J. Colloid Sci. 20 (1965) 893-911.
838 https://doi.org/https://doi.org/10.1016/0095-8522(65)90061-9.

839 [56] H.K. Palmer, R.C. Rowe, The application of mercury porosimetry to porous polymer
840 powders, Powder Technol. 9 (1974) 181-186. https://doi.org/https://doi.org/10.1016/0032-
841 5910(74)80030-6.

842 [57] J. Feng, W. Mo, S. Ma, Y. Wang, J. Yang, X. Su, G. Wang, M. Lin, Thermal shrinkage inhibition
843 mechanism of fumed silica based thermal insulating composite, Appl. Therm. Eng. 113 (2017)
844 749-755. https://doi.org/https://doi.org/10.1016/j.applthermaleng.2016.11.081.

845 [58] A. Bogaerts, Q.-Z. Zhang, Y.-R. Zhang, K. Van Laer, W. Wang, Burning questions of plasma
846 catalysis: Answers by modeling, Catal. Today 337 (2019) 3-14.
847 https://doi.org/https://doi.org/10.1016/j.cattod.2019.04.077.

848 [59] S. Kameshima, R. Mizukami, T. Yamazaki, L.A. Prananto, T. Nozaki, Interfacial reactions
849 between DBD and porous catalyst in dry methane reforming, J. Phys. D Appl. Phys. 51 (2018)
850 114006. https://doi.org/10.1088/1361-6463/aaad7d.

851 [60] K. Hensel, S. Katsura, A. Mizuno, DC microdischarges inside porous ceramics, IEEE Trans.
852 Plasma Sci. 33 (2005) 574-575. https://doi.org/10.1109/TPS.2005.845389.

853 [61] R. Snoeckx, R. Aerts, X. Tu, A. Bogaerts, Plasma-Based Dry Reforming: A Computational
854 Study Ranging from the Nanoseconds to Seconds Time Scale, J. Phys. Chem. C 117 (2013) 4957-
855 4970. https://doi.org/10.1021/jp311912b.

856 [62] B. Loenders, Y. Engelmann, A. Bogaerts, Plasma-Catalytic Partial Oxidation of Methane on
857 Pt(111): A Microkinetic Study on the Role of Different Plasma Species, J. Phys. Chem. C 125
858 (2021) 2966-2983. https://doi.org/10.1021/acs.jpcc.0c09849.

859 [63] E.C. Neyts, A. Bogaerts, Understanding plasma catalysis through modelling and simulation—
860 a review, J. Phys. D Appl. Phys. 47 (2014) 224010. https://doi.org/10.1088/0022-
861 3727/47/22/224010.

862 [64] K. Woo Seok, P. Jin Myung, K. Yongho, H. Sang Hee, Numerical study on influences of
863 barrier arrangements on dielectric barrier discharge characteristics, IEEE Trans. Plasma Sci. 31
864 (2003) 504-510. https://doi.org/10.1109/TPS.2003.815469.

865 [65] O. Tilmatine, L. Dascalescu, T. Zeghloul, K. Medles, A. Fatu, Study of the Influence of the
866 Different Parameters of the Atmospheric DBD Treatment on the Surface Roughness and the
867 Electric Potential Distribution Generated After the Tribocharging of Polypropylene, IEEE Trans.
868 Ind. Appl. 57 (2021) 4162-4169. https://doi.org/10.1109/TIA.2021.3081607.

869 [66] N. Rahemi, M. Haghighi, A.A. Babaluo, M.F. Jafari, S. Khorram, Non-thermal plasma assisted
870 synthesis and physicochemical characterizations of Co and Cu doped Ni/Al_2O_3 nanocatalysts
871 used for dry reforming of methane, Int. J. Hydrogen Energy 38 (2013) 16048-16061.
872 https://doi.org/https://doi.org/10.1016/j.ijhydene.2013.08.084.

873 [67] I. Luisetto, S. Tuti, C. Battocchio, S. Lo Mastro, A. Sodo, $Ni/CeO_2–Al_2O_3$ catalysts for the dry
874 reforming of methane: The effect of $CeAlO_3$ content and nickel crystallite size on catalytic
875 activity and coke resistance, Appl. Catal. A: Gen. 500 (2015) 12-22.
876 https://doi.org/https://doi.org/10.1016/j.apcata.2015.05.004.

877 [68] R.O. da Fonseca, A.R. Ponseggi, R.C. Rabelo-Neto, R.C.C. Simões, L.V. Mattos, F.B. Noronha,
878 Controlling carbon formation over Ni/CeO_2 catalyst for dry reforming of CH_4 by tuning Ni
879 crystallite size and oxygen vacancies of the support, J. CO2 Utilzation 57 (2022) 101880.
880 https://doi.org/https://doi.org/10.1016/j.jcou.2021.101880.

881   [69] F. Mirzaei, M. Rezaei, F. Meshkani, Coprecipitated Ni-Co Bimetallic Nanocatalysts for
882   Methane Dry Reforming, Chem. Eng. Technol. 37 (2014) 973-978.
883   https://doi.org/https://doi.org/10.1002/ceat.201300729.

884   [70] W. Wang, H.-H. Kim, K. Van Laer, A. Bogaerts, Streamer propagation in a packed bed plasma
885   reactor for plasma catalysis applications, Chem. Eng. J. 334 (2018) 2467-2479.
886   https://doi.org/https://doi.org/10.1016/j.cej.2017.11.139.

887